Journal of Molecular Catalysis A: Chemical 409 (2015) 149–161

Contents lists available at ScienceDirect

Journal of Molecular Catalysis A: Chemical

journal homepage: www.elsevier.com/locate/molcata

Photocatalytic degradation of ciprofloxacin by synthesized TiO_2 nanoparticles on montmorillonite: Effect of operation parameters and artificial neural network modeling

Aydin Hassani[a], Alireza Khataee[b,*], Semra Karaca[a,**]

[a] Department of Chemistry, Faculty of Science, Atatürk University, 25240 Erzurum, Turkey
[b] Research Laboratory of Advanced Water and Wastewater Treatment Processes, Department of Applied Chemistry, Faculty of Chemistry, University of Tabriz, 51666-16471 Tabriz, Iran

ARTICLE INFO

Article history:
Received 4 February 2015
Received in revised form 13 August 2015
Accepted 20 August 2015
Available online 24 August 2015

Keywords:
Ciprofloxacin
Nanocatalyst
Pharmaceuticals
Photocatalysis
TiO_2/MMT nanocomposite

ABSTRACT

TiO_2/MMT nanocomposite was synthesized and characterized by X-ray diffraction (XRD), fourier transform infrared spectroscopy (FTIR), scanning electron microscopy (SEM), Energy-dispersive X-ray spectroscopy (EDX), transmission electron microscopy (TEM), X-ray fluorescence (XRF) and Brunauer–Emmett–Teller (BET) techniques. The average size of TiO_2 nanoparticles was decreased from 60–80 nm to 40–60 nm through the immobilization on MMT. The main influential factors such as the TiO_2/MMT dose, ciprofloxacin (CIP) concentration, pH of the solution, UV light regions, reusability of the catalyst and electrical energy determination were studied. The addition of radical scavengers (e.g. chloride, iodide, sulfate and bicarbonate) and enhancers (e.g. hydrogen peroxide, potassium iodate and peroxydisulfate) on the degradation efficiency was studied. The predicted data from the designed artificial neural network model were found to be in a good agreement with the experimental data (R^2 = 0.9864). The main intermediates of CIP degradation were determined by GC–Mass spectrometry.

1. Introduction

Currently, due to their remarkable utilization and hazardous biological and ecotoxicological effects, personal care products (PCPs) and pharmaceuticals can be regarded as one of the major groups of water contaminants. It is known that pharmaceuticals and their metabolites get into wastewater treatment plants (WTP); however, it should be noted that some of them may not be completely removed or transformed during conventional wastewater treatment methods. Wastewaters from industries, hospitals and domestic sites effluents are directly thrown into the surface and ground waters without any previous decontamination treatment. This can result in pollution and disturbing effects [1,2]. Recently, Voogt et al. [3] have proposed a list of the most important 44 pharmaceuticals related to the water cycle on the basis of their toxicity, physicochemical properties, occurrence, consumption persistence and resistance to treatment. As can be observed in the related literature, most of these pharmaceuticals, because of their high resistance to conventional wastewater treatments methods, are persistent in water cycles and therefore, become omnipresent in the environment. Therefore, the effect of these pharmaceuticals and their metabolites on the environment, their genotoxicity and acute toxicity have been the subject of serious scientific research [4]. According to the previous studies in the field, advanced oxidation processes (AOPs) are well-accepted technologies for the removal of a wide variety of persistent organic pollutants from water and wastewater [5–8]. Titanium dioxide (TiO_2) is a predominant photocatalyst for environmental application due to its exceptional properties such as higher photocatalytic oxidation ability, nonphotocorrosiveness, chemical and biological inertness, nontoxicity and low cost characteristics [9–11]. However, there are still some inherent drawbacks such as small specific surface area, low adsorption ability, difficult recovery and the agglomeration phenomenon of suspended powder TiO_2 at high loadings, all limiting its practical application in the wastewater treatment [12]. This problem can be tackled through the immobilization of TiO_2 on the surface of supported materials without the loss of activity. Consequently, various kinds of supports, such as silica, alumina, glass plate, zeolite and clay, have been widely employed used to immobilize the catalysts [13–17]. As can be understood from the literature, clay and clay

* Corresponding author. Fax: +98 41 33340191.
** Corresponding author. Fax: +90 442 2360948.
E-mail addresses: a_khataee@tabrizu.ac.ir, ar_khataee@yahoo.com (A. Khataee), semra_karaca@yahoo.com, skaraca@atauni.edu.tr (S. Karaca).

http://dx.doi.org/10.1016/j.molcata.2015.08.020
1381-1169/

Table 1
Characteristics of the ciprofloxacin (CIP).

Chemical structure	Molecular formula	Mw (g mol^{-1})	λ_{max}(nm)	Therapeutic group	Solubility in water (mg mL^{-1})
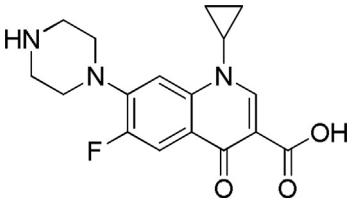	$C_{17}H_{18}FN_3O_3$	331.346	276	Antibiotic	30

based photocatalysts are regarded as promising and appropriate materials for this purpose because they are chemically inert, resistant to deterioration, inexpensive and commercially available in larger quantities [14,18]. In recent years, clays such as montmorillonite, rectorite and kaolinite have been of great interest for their applicability in wastewaters decontamination. It is known that clay minerals possess layer structures, high porosity, large surface areas, exchangeable cations and swellable properties [19,20]. The previous studies in the field have revealed that dispersion TiO_2 particles into layered clays (TiO_2 pillared clay) and/or the immobilization of TiO_2 on the surface of MMT can improve catalyst efficiency as such composite structures are known to stabilize TiO_2 particles and keep most of the surface of TiO_2 crystals accessible to various molecules [14,21]. Ciprofloxacin (CIP), which is a second generation fluoroquinolone, is an antibacterial agent that can be very persistent in aquatic environments. The chemical name of CIP is 1-cyclopropyl-6-fluoro-1, 4-dihydro-4-oxo-7-(1-piperazinyl)-3-quinolinecarboxylic acid. Because of the poor biodegradability of CIP, the removal of this pollutant by chemical oxidation has been attempted. In recent years, degradation of CIP has been investigated using photo-Fenton [22], sonolysis [23], UV/$S_2O_8^{2-}$ [24], UV/H_2O_2 [25] and adsorption [26] processes. TiO_2 nanoparticles were synthesized and immobilized on the surface of Montmorillonite K10 (MMT) in the present study for photocatalytic degradation of CIP as the target pollutant. To this aim, X-ray diffraction (XRD), Fourier transform infrared spectroscopy (FTIR), scanning electron microscopy (SEM), Energy-dispersive X-ray spectroscopy (EDX), transmission electron microscopy (TEM), X-ray fluorescence (XRF) and Brunauer–Emmett–Teller (BET) were employed to characterize the as-prepared nanocomposite. Accordingly, CIP was used as the model organic pollutant to evaluate the photocatalytic performance of TiO_2/MMT nanocomposite during UV-C radiation. To the best of our knowledge and on the basis of the literature review, it can be understood that the use of hydrothermal method for the preparation of TiO_2/MMT nanocomposite and its potential for the photocatalytic degradation of CIP have not been investigated yet. More clearly, this study addressed the effect of various parameters such as catalyst dosage, the initial CIP concentration, the effect of UV light region, the initial pH, the presence of various radical scavengers and process enhancers on the promoted photocatalytic process. Additionally, artificial neural network (ANN) was utilized to model the photocatalytic process.

2. Experimental

2.1. Materials

Montmorillonite K10 (MMT) was purchased from Sigma–Aldrich Co. (USA). The cation exchange capacity (CEC) of the clay (120 meq/100 g) was determined by the ammonium acetate method [27]. Cetyltrimethylammonium bromide (CTAB) was purchased from Sigma–Aldrich Co. (USA). Tetraethyl orthotitanate (TEOT) is a precursor of Ti was purchased from Sigma–Aldrich Co. (USA). All other chemicals and reagents, being of analytical grade, were purchased from Merck (Germany) and used without further purification. Ciprofloxacin was supplied by Farabi pharmaceutical company (Iran). The specifications of CIP are shown in Table 1.

2.2. Synthesis of TiO_2/MMT nanocomposite and characterization

TiO_2/MMT nanocomposite was prepared through the synthesis of TiO_2 nanoparticles on the surface of the MMT. Fig. 1 shows the schematic of the preparation method carried out in two stages. Pure TiO_2 nanoparticles were synthesized by the same procedure without the addition of MMT.

The XRD spectrum of the synthesized TiO_2/MMT nanocomposite was obtained using a PANalytical X'Pert PRO diffractometer (Germany) with Cu–Ka radiation (45 kV, 40 mA, 0.15406 nm). The chemical composition of the MMT and TiO_2/MMT was determined by X-ray fluorescence (XRF) (Rigaku ZSX Primus II, Japan). Scanning electron microscope (SEM) model MIRA3 FEG-SEM Tescan (Czech) was used to detect the morphology and particle sizes of the samples. The TiO_2, MMT and TiO_2/MMT samples were analyzed with a Fourier transform infrared spectroscopy (FTIR) model Tensor 27, Bruker (Germany), in a wavenumber range of 4000–400 cm^{-1} using the KBr pellet technique. The transmission electron microscopy (TEM) image was conducted using a Cs-corrected high-resolution TEM (Zeiss-EM10C, Germany) that operated at 100 kV. For this analysis, the synthesized TiO_2/MMT sample was dispersed in ethanol using ultrasonic vibration (Bandelin Sonorex, Germany) for 15 min; then a drop of the dispersed sample was placed on a copper grid coated with a layer of amorphous carbon to record the TEM image. Textural properties of the MMT, TiO_2 and TiO_2/MMT samples were determined from N_2 adsorption–desorption isotherms at 77 K on a Gemini 2385 nitrogen adsorption apparatus (Micromeritics Instruments, USA) and their pore structure was analyzed using Brunauer–Emmett–Teller (BET) and Barrett–Joyner–Halenda (BJH) methods. Particle size distributions were conducted using Malvern Mastersizer 2000 (UK).

2.3. Photocatalytic degradation setup and procedure

The experimental set-up for the photocatalytic degradation of CIP by immobilized TiO_2 nanoparticles on MMT is schematically shown in Fig. 2. Photocatalysis of CIP was performed in a batch photoreactor with a 500 mL working volume. A 16 W UV-A, UV-B or UV-C lamp (Sylvania, Japan) was applied as the light source. Batch studies were performed to evaluate the effect of CIP concentration, TiO_2/MMT dose, the initial pH, UV light region, different scavengers and enhancers on degradation efficiency. For each photocatalytic experiment, 500 mL of an aqueous solution containing CIP in the range of 5–25 mg L^{-1} with 0.025–0.150 g L^{-1} of the TiO_2/MMT nanocomposite was added in the reaction vessel. The UV-A, UV-B or UV-C lamp was turned on at the beginning of each experiment. The pH of the solution was set to the desired value

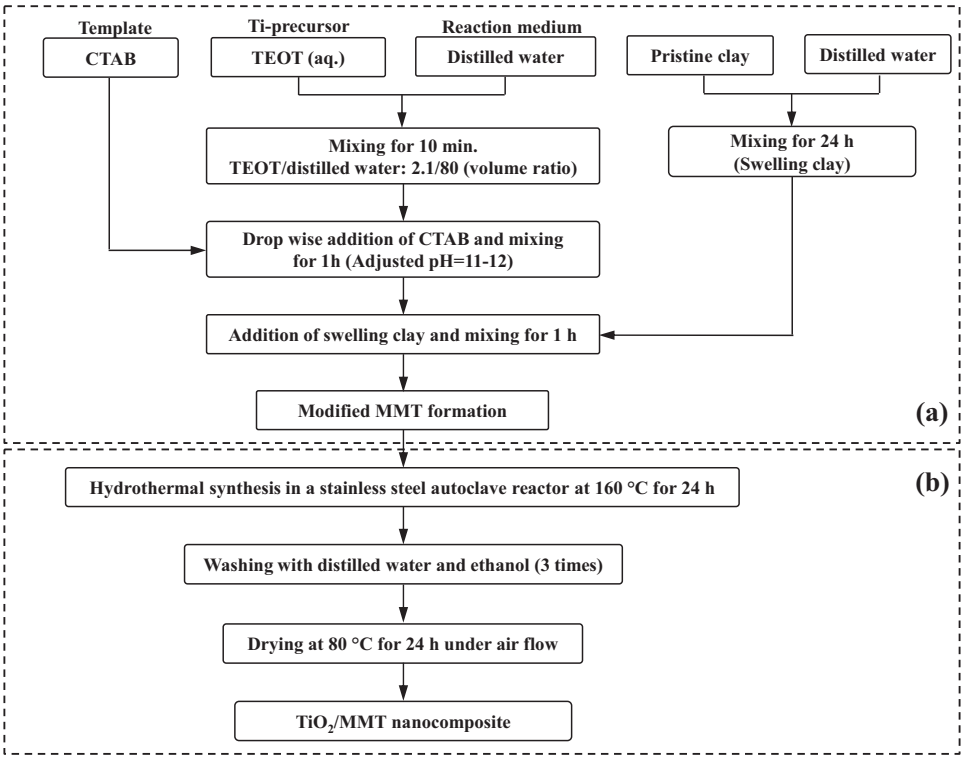

Fig. 1. A flow chart used for the preparation of the TiO_2/MMT nanocomposite: (a) precursor preparation and (b) nanocomposite forming.

with H_2SO_4 and NaOH (0.1 M). The solution pH was regulated with a Mettler Toledo pH meter (China). 5 mL samples were taken from the reactor at different intervals and residuals concentration of CIP was measured using Varian Cary 100 UV–vis spectrophotometer (Australia) at the maximum wavelength of 276 nm. Degradation efficiency (%) = $[(C_0-C_t)/C_0] \times 100$ was used to determine the degradation of CIP, where C_0 was the initial concentration of CIP solution and C_t was its concentration after a certain time (t). Adsorption experiments were conducted using the method applied for photocatalytic degradation experiment without UV radiation. The zero point of charge (pH_{zpc}) of the TiO_2/MMT nanocomposite was measured using the method described by Bessekhouad et al. with some modifications [28]. In this approach, 500 mL 0.01 M NaCl was prepared and divided into eight solutions with the pH ranging from 3 to 10. 0.2 g of the catalyst was added to each solution. Finally, the final pH of each solution was measured after 48 h shaking and plotted against the initial pH to determine the pH_{zpc} of the catalyst. Electrophoretic mobility and the surface charge of the samples were carried out with the relation of the zeta potential measurements. Zeta potentials of the samples were measured using a Zeta Meter 3.0+ (Zeta-Meter, Inc., USA). The zeta potential of pure MMT, TiO_2 and TiO_2/MMT was obtained to be −30.7, +21.06 and −16.4 mV, respectively.

2.4. ANN modeling

It can be inferred from the previous studies that the artificial neural networks (ANN) have been widely employed to investigate the relative importance of parameters during photocatalytic degradation process [29]. ANN modeling was employed in this study using ANN toolbox of Matlab (MathWorks, Ine., USA) mathematical software. Accordingly, a three-layer feed-forward back propagation neural network which consisted of input, output and intermediate hidden layers was used for modeling the photocatalytic degradation of CIP. The layers, the number of neurons as the processing unit of ANN in each layer and the transfer functions between the layers form neural network topology were taken in to account [30]. The linear transfer function was also utilized in the hidden and output layers. The input layer was in accordance with four experimental parameters including the initial CIP concentration ($mg\,L^{-1}$), irradiation time (min), catalyst dosage ($g\,L^{-1}$) and the initial pH. The output layer, on the other hand, was the degradation efficiency (%). All data obtained from the experiments (X_i) were scaled in 0.1–0.9

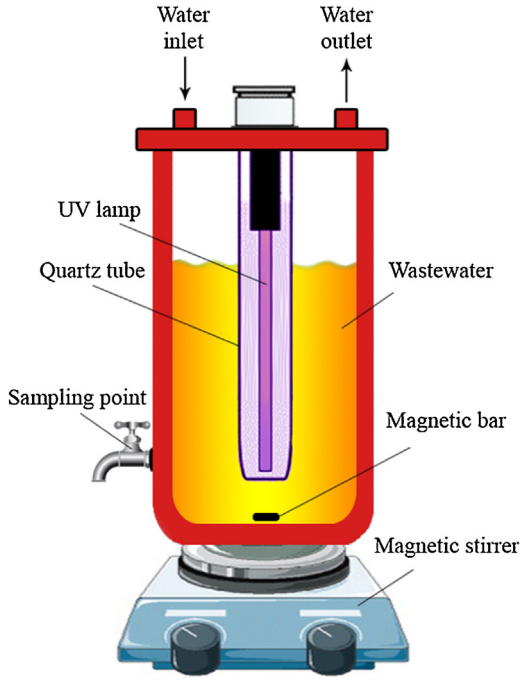

Fig. 2. Schematic representation of the reactor used for different processes.

range (X_i) using Eq. (1), and then divided into training, validation and test sets with a ratio of 72%, 24% and 24%, respectively.

$$x_i = 0.6\left(\frac{X_i - \min(X_i)}{\max(X_i) - \min(X_i)}\right) + 0.2 \quad (1)$$

where $\min(X_i)$ and $\max(X_i)$ were the extreme values of the input variables X. The mean square error (MSE) was used as the error function [29]. At the same time, the relative importance of each input variable on the output variable was calculated by Eq. (2).

$$I_j = \frac{\sum_{m=1}^{m=N_h}((|W_{jm}^{jh}|/\sum_{k=1}^{N_i}|W_{km}^{ih}|) \times |W_{mn}^{ho}|)}{\sum_{k=1}^{k=N_i}\{\sum_{m=1}^{m=N_h}(|W_{km}^{ih}|/\sum_{k=1}^{N_i}|W_{km}^{ih}|) \times |W_{mn}^{ho}|)\}} \quad (2)$$

where I_j was the relative importance of j_{th} input variable on the output variable and N_i and N_h were the numbers of input and hidden neurons, respectively. W is the connection weight, and the superscripts i, h and o refer to the input, hidden and output layers, respectively. Also, subscript k, m and n refer to the input, hidden and output neurons, respectively.

3. Results and discussion

3.1. Structural analysis of TiO_2/MMT nanocomposite

Table 2 shows the chemical composition analysis of the pure MMT and TiO_2/MMT nanocomposite. As can be seen, most of the material in MMT consisted of SiO_2 (66.9 wt.%) followed by Al_2O_3 (13.8 wt.%). Titanium oxide was also observed in low content. According to the obtained results, the TiO_2 content of 58.5 wt.% in the TiO_2/MMT nanocomposite was higher than that in the pure MMT. It was confirmed by chemical composition analysis that a considerable amount of TiO_2 species was introduced and hybridized with MMT. Fig. 3(a and b) shows X-ray diffraction patterns recorded for the raw montmorillonite and TiO_2/MMT nanocomposite, respectively. The MMT clay depicts the diffraction peak at 2θ of 19.9°, 35.0°, 53.9° and 61.7° and the reflections at 2θ of 20.9°, 26.7°, 36.5°, 42.4°, 45.8°, 50.2°, 59.9° and 68.1° which are attributed to the quartz phase (see Fig. 3a) [31–33]. As shown in Fig. 3b, the basal spacing of montmorillonite was changed by the intercalation of TiO_2 nanoparticles. The d_{001} peaks were changed and new peaks related to the basal spacing were observed around at 2θ of 8.5° and 17.50°. This clearly indicated the enlargement of the basal spacing of the clay as a result of the interaction between MMT and TiO_2 nanoparticles. Additionally, it was shown that TiO_2 nanoparticles were present within the interlayer space of the MMT clay. On the other hand, as evidenced in Fig. 3b, the diffraction peaks at 2θ of 8.5°, 17.5°, 19.5°, 35.0° and 61.6° were characteristic of MMT. The similar characteristic peaks were observed for quartz according to the XRD pattern of the raw MMT (see Fig. 3a). Moreover, the XRD pattern of TiO_2/MMT demonstrated a characteristic diffraction peak at 2θ of 25.4°, 37.7°, 48.1°, 55.1° and 75.3°, thereby indicating the presence of anatase phase [14,32]. It should be noted that for both samples, peaks corresponding to quartz were also unequivocally identified; this has already been shown by the previous studies [33–35]. The spectrum totally agrees with the previously reported literature for the montmorillonite and the modified clay [31,32,36]. SEM analysis was used to investigate the morphology of the MMT, TiO_2 and TiO_2/MMT particles. As can be seen in Fig. 4a, MMT had an uneven structure with non-uniform size distribution. The pure MMT with some phase separations and cracks was seen, generally showing a heterogeneous surface morphology. The SEM image of synthesized TiO_2 particles is presented in Fig. 4b. The particle size distribution of TiO_2 nanoparticles was calculated using Manual Microstructure Distance Measurement software (Nahamin Pardazan Asia Co., Iran). As depicted in Fig. 4e, the particle size distribution plot of TiO_2 nanoparticles showed that most of the nanoparticles range from 60 to 80 nm with the frequency of 38.09%. Fig. 4c shows that the SEM image of TiO_2/MMT nanocomposite approved the presence of TiO_2 particles on the surface of MMT. Fig. 4f exhibits the size distribution of TiO_2 nanoparticles, indicating that most of the TiO_2 particles in TiO_2/MMT nanocomposite are in the range of 40–60 nm with the frequency of 75%. The results revealed that the average size of TiO_2 nanoparticles immobilized on the surface of MMT was smaller than that of pure TiO_2 nanoparticles. The particle size distributions of TiO_2/MMT nanocomposite were measured using the laser light diffraction method. According to the obtained results, size rangeability of TiO_2/MMT varied from 0.04 to 20 μm, with the majority of the nanocomposite particles being in the size range of 0.1–0.2 μm. The EDX pattern of TiO_2/MMT is illustrated in Fig. 4d. The results indicated that the TiO_2/MMT contained C, O, Si, Ti, Mg, Al, Na and K, providing evidence that TiO_2 nanoparticles were formed and immobilized on the surface of the MMT. According to the SEM analysis, it could be deduced that hydrothermal method utilized in the present work was a reliable means for the preparation of TiO_2/MMT nanocomposites with predictable results.

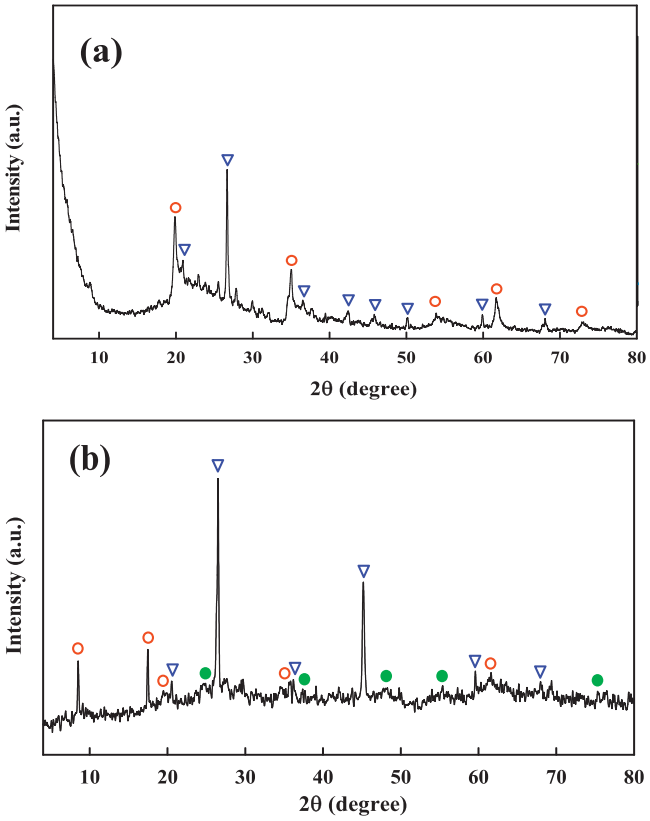

Fig. 3. XRD patterns of (a) MMT and (b) TiO_2/MMT nanocomposite: O montmorillonite, ∇ quartz, and ● anatase.

TEM analysis was used to investigate the more structural information. Fig. 5 illustrates the immobilized state of TiO_2 particles on the MMT. There were various well-distributed small particles within the MMT layers, thereby indicating the good intercalation of TiO_2 particles into the interlayer of MMT and the destruction of the ordered structure of MMT clay. Also, the deposited TiO_2 nanoparticles were aggregated on the surface of the MMT particles.

FTIR analysis was performed to investigate the variations on the functional groups of TiO_2 and MMT during the preparation of TiO_2/MMT nanocomposite. Fig. 6 shows FTIR spectra of MMT, TiO_2 and TiO_2/MMT, respectively. As shown in Fig. 6a, the pure

Table 2
Chemical composition of MMT and TiO_2/MMT samples.

Sample	Chemical compositions (wt.%)								
	SiO_2	Al_2O_3	Fe_2O_3	K_2O	MgO	CaO	Na_2O	TiO_2	Others
MMT	66.90	13.80	2.75	1.65	1.58	0.29	0.15	0.44	12.44
TiO_2/MMT	28.30	7.58	1.55	0.883	0.670	0.161	2.27	58.50	0.086

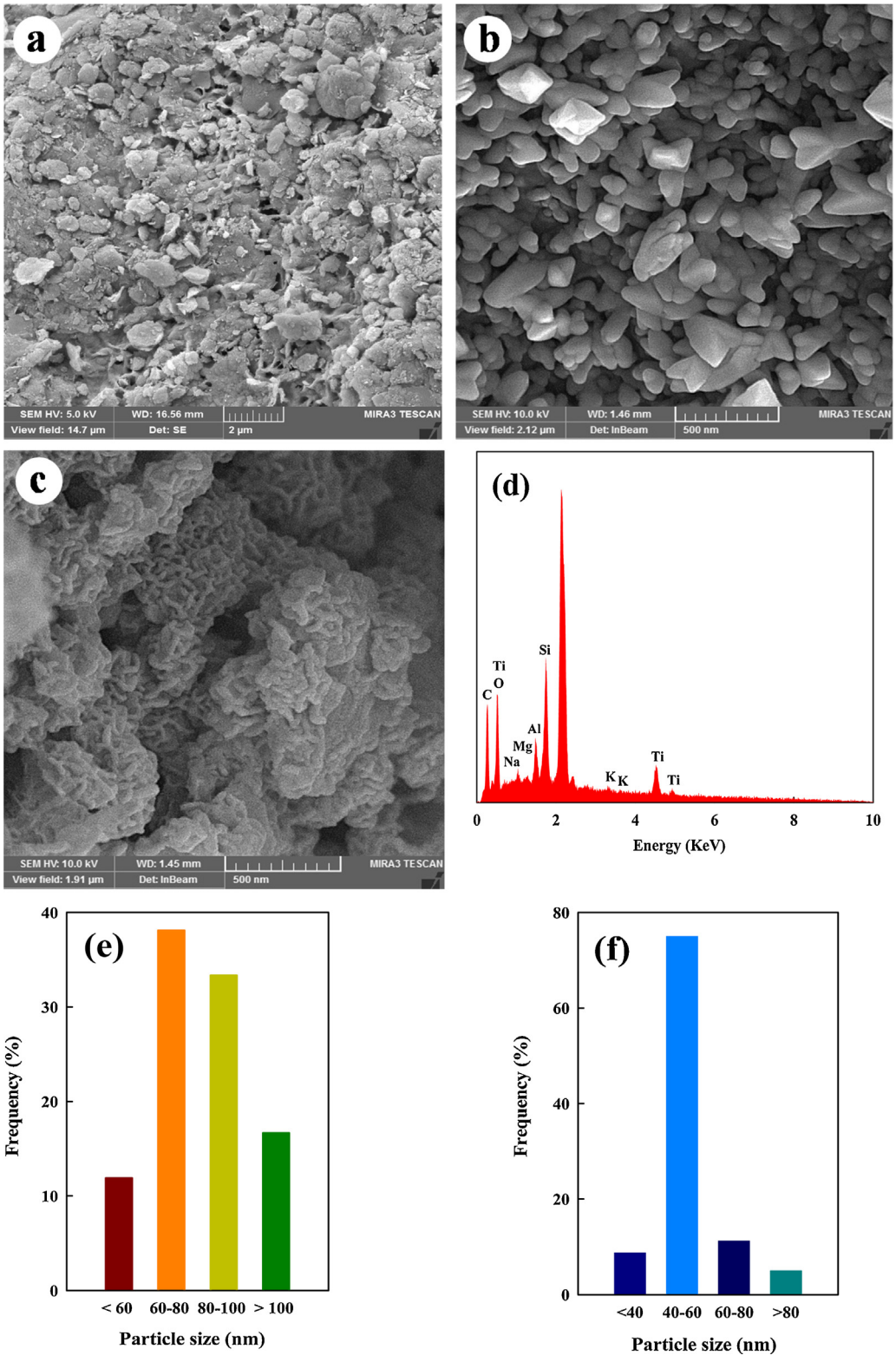

Fig. 4. SEM micrographs of (a) MMT, (b) TiO_2, (c) TiO_2/MMT, (d) EDX elemental microanalysis of TiO_2/MMT sample, (e) distribution of TiO_2 particles size in pure TiO_2 sample and (f) distribution of TiO_2 particles size in TiO_2/MMT sample.

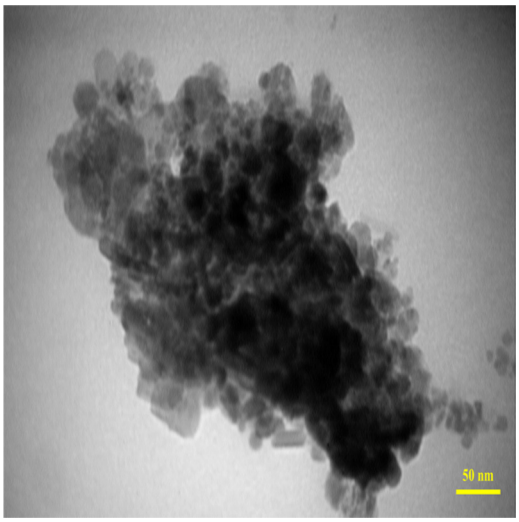

Fig. 5. TEM photograph of TiO_2/MMT nanocomposite.

MMT had a weak –OH stretching vibration of crystalline water at 3620 cm^{-1} and a strong broad band at 3420 cm^{-1}, corresponding to the stretching vibration of the —OH group and the interlayer water molecules. The bending vibration of water molecules caused a peak at 1630 cm^{-1}. The band around 1050 cm^{-1} was attributed to asymmetric stretching vibration of Si—O in the pure MMT [36,37]. Several bands around 912 cm^{-1} and 785 cm^{-1} were attributed to the stretching vibration of Al—O. The bands around 472 cm^{-1} and 530 cm^{-1} corresponded to Si—O—Si deformation and Al—O—Si deformation, respectively [38]. The FTIR spectrum of TiO_2 is shown in Fig. 6b. The peaks around 480 cm^{-1} corresponded to the stretching vibration of Ti—O band [39]. The bands at 1630, 2845, 2924 and 3420 cm^{-1} were attributed to interlayer water molecules, symmetric stretching vibration of C—H and stretching vibration of —OH, respectively. FTIR spectrum of TiO_2/MMT nanocomposite is presented in Fig. 6c. As it is obvious, the development of new absorption peak at 935 cm^{-1} could be attributed to Ti—O—Si stretching vibration [40]. Moreover, the disappearance or weak intensities of the bands in the range of 460–530 cm^{-1} and 1050 cm^{-1} clearly indicated that the basic structure of the MMT was destroyed during the preparation of this nanocomposite.

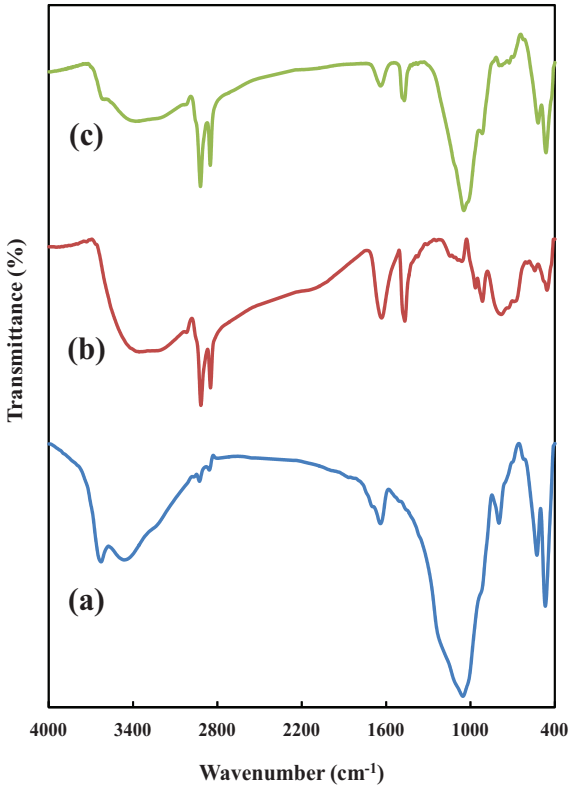

Fig. 6. FTIR spectrum of (a) MMT, (b) TiO_2 and (c) TiO_2/MMT.

Table 3
Surface area and average pore size characteristics of MMT, TiO_2 and TiO_2/MMT nanocomposite samples.

BJH total volume[c] ($cm^3\ g^{-1}$)	Pore size[b] (nm)	BET surface area[a] ($m^2\ g^{-1}$)	Sample
0.452–0.456	2.62	279.278	MMT
0.035–0.036	4.61	8.813	TiO_2
0.105–0.106	3.87	53.058	TiO_2/MMT

[a] Obtained by BET measurement.
[b] Calculated by the BJH (desorption) method using N_2 adsorption isotherm.
[c] Obtained by the BJH method.

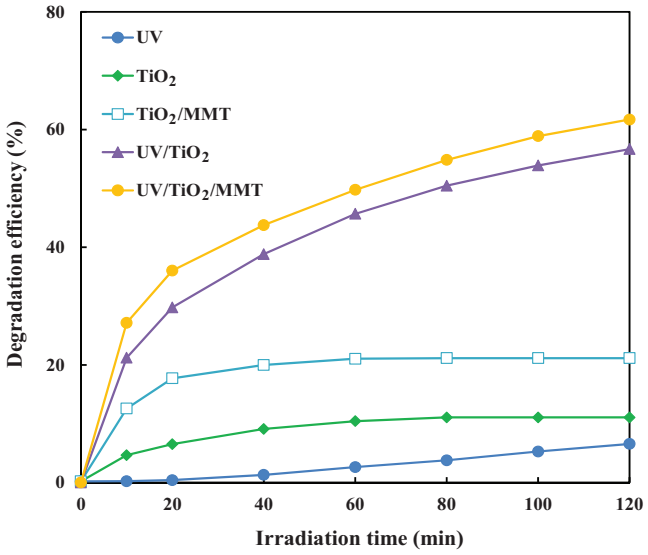

Fig. 7. Comparison of different processes in the photocatalytic degradation of ciprofloxacin at different times. Conditions: $[Catalyst]_0 = 0.1\ g\ L^{-1}$, $[CIP]_0 = 20\ mg\ L^{-1}$ and pH 5.

Table 3 shows the BET specific surface area and pore parameters of the synthesized catalysts. The specific surface area of the pure TiO_2 was 8.813 $m^2\ g^{-1}$. After the immobilization of TiO_2 on the surface of MMT, an increase in BET value and total volume was observed for TiO_2/MMT. On the other hand, the pore size was decreased from 4.61 nm to 3.87 nm for TiO_2 and TiO_2/MMT, respectively. These results indicated that the synthesis of TiO_2 on the surface of MMT by hydrothermal method led to the production of nanocomposite with high surface area and total volume in comparison to those of pure TiO_2. The decrease in the specific surface area of TiO_2/MMT nanocomposite, as compared with that of MMT, could be attributed to the collapse of pores of MMT and the exfoliation of MMT in TiO_2 matrix as a result of the settlement of TiO_2 interlayer galleries of MMT. In addition, the change in surface area may be due to occupancy of the internal surface of pores by TiO_2 nanoparticles. Similar observation with various catalysts reported in the literature [41–44].

3.2. Comparison of CIP degradation by different processes

Fig. 7 compares the removal of CIP with the initial concentration of 20 mg L^{-1} by different processes. The results indicated 6.57% of CIP degradation by direct photolysis under UV-C radiation. Hence, direct photolysis alone could not be used as an impressive procedure for the removal of CIP from aqueous solutions. As can be seen in Fig. 7, the removal of CIP via adsorption onto TiO_2 and TiO_2/MMT was lower in comparison to photocatalysis process. The improved efficiency in removing CIP by UV/TiO_2 process could be ascribed to the production of hydroxyl radicals, which acted as a powerful oxidizing agent. Furthermore, the obtained results demonstrated that the photocatalysis of CIP in the presence of TiO_2/MMT was higher than that of TiO_2. It could be attributed to the increase in the surface area of TiO_2/MMT, rather than TiO_2, as it led to the remarkable enhanced adsorption capability of the catalyst. The best results were achieved in UV/TiO_2/MMT system. UV/TiO_2/MMT was employed as the best option for conducting the rest of the experiments. Our findings provided results similar to those of previous studies with regard to the photocatalysis of different pollutants [35,45].

3.3. The effect of TiO_2/MMT dosage

Catalyst dosage is an important parameter in heterogeneous photocatalytic reaction [46]. In order to determine the effect of catalyst dosage on the photodegradation of CIP, experiments were carried out by varying the amount of TiO_2/MMT from 0.025 g L^{-1} to 0.150 g L^{-1} (Fig. 8). The photodegradation efficiency was increased with an increase in TiO_2/MMT dosage up to 0.1 g L^{-1} and decreased thereafter. Increasing the amount of photocatalyst from 0.1 g L^{-1} to 0.150 g L^{-1} resulted in decreasing the photodegradation efficiency from 61.70% to 54.30% at the reaction time of 120 min, respectively. By increasing the catalyst dosage, the surface area was increased, leading to an increase in the production of reactive species [47,48]. However, more catalyst dosage would also induce greater aggregation of the catalyst and decrease the total active surface area, thereby leading to a reduction in the degradation efficiency. Moreover, due to an increase in the turbidity of the solution, reduction in the degree of light penetration through the solution could take place [7,49]. Therefore, other experiments were carried out with 0.1 g L^{-1} TiO_2/MMT to avoid the excessive usage of the catalyst.

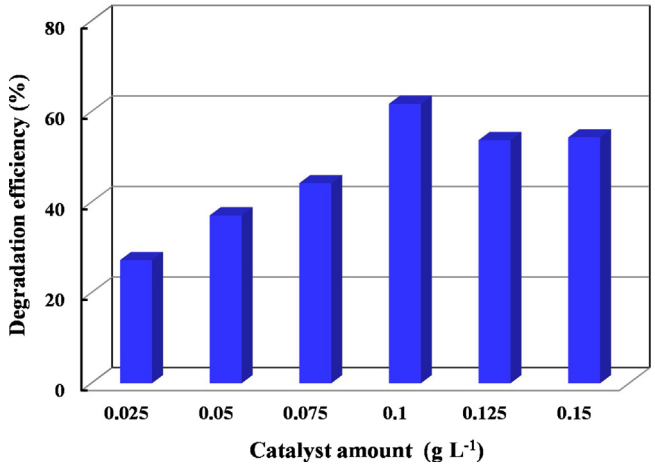

Fig. 8. The effect of TiO_2/MMT amount on the photodegradation efficiency of ciprofloxacin at the irradiation time of 120 min. Conditions: $[CIP]_0$ = 20 mg L^{-1} and pH 5.

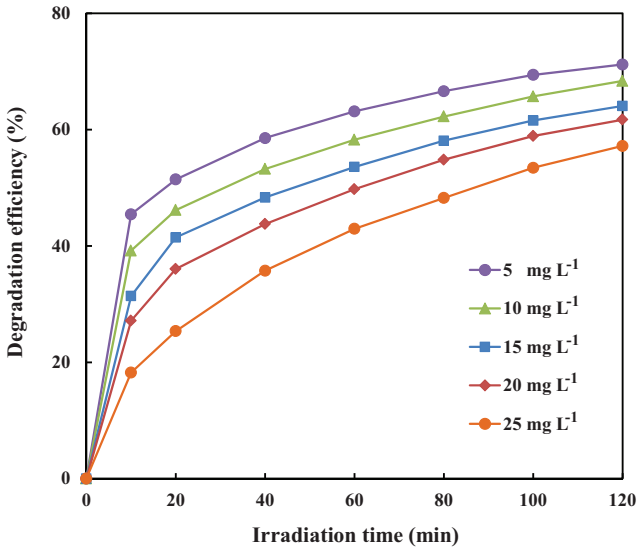

Fig. 9. The effect of initial ciprofloxacin concentration on photodegradation efficiency by TiO_2/MMT. Conditions: $[Catalyst]_0$ = 0.1 g L^{-1} and pH 5.

3.4. The effect of the initial CIP concentration

One of the most important things is to study the dependence of photocatalytic degradation on the concentration of water contaminants [50,51]. The degradation of CIP was studied by changing its initial concentration in the range of 5–25 mg L^{-1}. As can be seen in Fig. 9, the degradation efficiency was decreased from 71.2% to 57.2% with an increase in the initial CIP concentration from 5 mg L^{-1} to 25 mg L^{-1}. When the initial CIP concentration was decreased, the probability of the reaction between CIP and oxidizing species was increased, leading to an improvement of photodegradation efficiency. However, the excess CIP concentration reduced photodegradation efficiency. On the other hand, at low CIP concentration, excess active adsorption sites on the photocatalyst surface could interact with the relatively insufficient CIP molecules in the solution. Consequently, the degradation efficiency of CIP was high. However, with increasing the pollutant in the aqueous solution, there was a surplus. In this case, only parts of CIP could interact with limited active sites on the photocatalyst surface, thereby causing lower photodegradation efficiency of CIP at higher initial concentration. In addition, according to the Beer-Lambert law, as the initial CIP concentration was increased, the path length of photons entered the solution decrease, thereby resulting in lower photon adsorption on catalyst particles and consequently decreasing the generation of hydroxyl radical [52,53]. Thus, the photodegradation efficiency was gradually decreased as a result of increasing CIP concentration.

Literature review revealed that the kinetic model for heterogeneous photocatalytic was in accordance with the Langmuir-Hinshelwood kinetic expression [54,55]. This model for CIP degradation can be written as follows:

$$r = -\frac{d[C]}{dt} = K_c \frac{K_{ads}[C]}{1+K_{ads}[C]_0} = K_{obs}[C] \quad (3)$$

$$\frac{1}{K_{obs}} = \frac{1}{K_c K_{ads}} + \frac{[C]_0}{K_c} \quad (4)$$

where $[C]_0$ is the initial concentration of CIP (mg L^{-1}), K_{ads} is the Langmuir–Hinshelwood adsorption equilibrium constant (L mg^{-1}), k_c is the rate constant of surface reaction (mg L^{-1} min^{-1}), and k_{obs} is the pseudo-first-order rate constant (min^{-1}). When initial concentrations were plotted versus $\frac{1}{K_{obs}}$, the rate constant of surface reaction and the adsorption equilibrium constant were

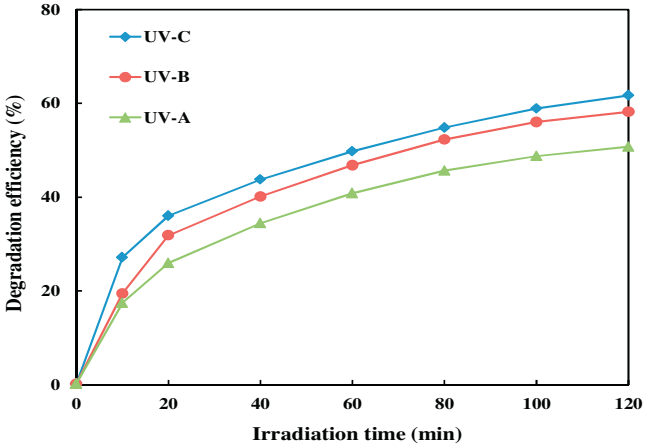

Fig. 10. The effect of UV light kind on the photodegradation efficiency of ciprofloxacin. Conditions: $[Catalyst]_0 = 0.1\ g\ L^{-1}$, $[CIP]_0 = 20\ mg\ L^{-1}$ and pH 5.

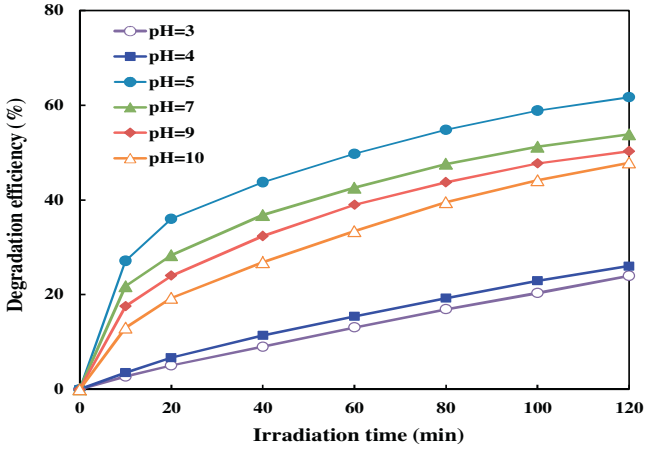

Fig. 11. The effect of pH on the photodegradation efficiency of ciprofloxacin. Conditions: $[Catalyst]_0 = 0.1\ g\ L^{-1}$, and $[CIP]_0 = 20\ mg\ L^{-1}$.

determined to be $k_c = 0.634\ mg\ L^{-1}\ min^{-1}$ and $K_{ads} = 0.0138\ L\ mg^{-1}$, respectively. The good regression coefficient ($R^2 = 0.9971$) indicated that the photocatalytic degradation of CIP by the TiO_2/MMT fitted the Langmuir–Hinshelwood kinetic expression well.

It should be noted that the main operational cost of the photocatalytic degradation process is relevant to the electrical energy consumption as it is considered an economical factor [56]. Electrical energy consumption ($KWh\ m^{-3}$) of photocatalytic process at optimal experimental conditions is reported in Table 4. As depicted in Table 4, the lowest E_{EO} consumption could be attributed to UV/TiO_2/MMT process.

3.5. The effect of the type of UV light source

In order to evaluate the impact of the kind of UV light on CIP removal in the photocatalytic process, different UV light regions including UV-A, UV-B and UV-C were employed (Fig. 10). The degradation efficiency of CIP was increased in the order of UV-A < UV-B < UV-C. The results could be explained in terms of the energy of photons emitted from UV-C lamp as it was higher than that of UV-B and UV-A. Hence, photogeneration of e^-/h^+ pairs under UV-C radiation was high and consequently, more reactive radicals were developed for the degradation of the target pollutant [57].

3.6. The effect of the initial pH

The solution pH is one of the important parameters that can markedly affect the photocatalytic process. In the present work, the effect of the initial pH on the photocatalytic degradation efficiency of CIP was studied in the pH range of 3–10 (Fig. 11). The results indicated that the degree of photodegradation efficiency was increased with increasing the solution pH up to 5 and then decreased. Explaining the pH effect on the photocatalytic process is a very laborious task because of its multiple roles such as electrostatic interactions between the semiconductor surface, solvent molecules, substrate and charged radicals formed during the reaction process. The pH at which the surface of a catalyst is uncharged is defined as the zero point charge (pH_{zpc}). The pH_{zpc} of TiO_2/MMT was obtained to be 8.4. The CIP has two pK_a values (5.9 and 8.89). It can exist as a cation ($CIP^{0,+}$), zwitterions ($CIP^{-,+}$) and anion ($CIP^{-,0}$) at different pHs [58,59]. When pH is lower than 5.9, CIP is in cationic species, while it exists as anionic form when pH value is higher than 8.89. At the low pH values, the decrease in photodegradation efficiency could be attributed to the favored hydrogen ions adsorption and/or scavenger effect of Cl^- ions produced from HCl used in adjusting pH, as well as the repelling effect between the positively charged surface of catalyst and CIP. Furthermore, the low photodegradation efficiency at more acidic pH (for example, at 3) may be related to the decomposition and corrosion of catalyst in acidic medium [60]. On the other hand, both TiO_2/MMT and CIP were negatively charged in basic conditions, leading to electrostatic repulsion between them and the low photodegradation efficiency of CIP. In the case of pH 5 (the natural pH of CIP), adsorption efficiency was the highest and the surface of TiO_2/MMT was still in the positive form and the CIP was in its neutral form. In other words, it could be concluded that adsorption occurred through ion exchange mechanism depending on the entropy factor. Accordingly, these results, as mentioned above, showed that the natural pH of CIP facilitated the adsorption of the CIP molecule and improved photocatalytic degradation.

3.7. The effect of the presence of radical scavengers

To assess the effect of the presence of radical scavengers on the photocatalytic degradation of CIP, bicarbonate, sulfate, iodide and chloride, which are normally present in water, were employed. As shown in Fig. 12, at the irradiation time of 120 min, the degradation efficiency was decreased from 61.70% to 52.87%, 42.94%, 39.86% and 25.83% in the presence of bicarbonate, sulfate, iodide and chloride, respectively. Accordingly, the order of the inhibitory effect of different radical scavengers was found to be as $Cl^- > I^- > SO_4^{2-} > HCO_3^-$.

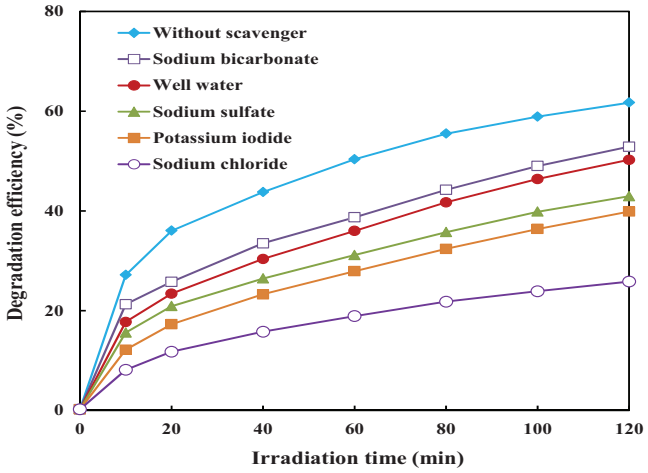

Fig. 12. The effect of the presence of different salts (as radical scavengers) on the degradation efficiency of ciprofloxacin. Conditions: $[Catalyst]_0 = 0.1\ g\ L^{-1}$, $[Radical\ scavenger]_0 = 20\ mg\ L^{-1}$, $[CIP]_0 = 20\ mg\ L^{-1}$, and pH 5.

Table 4
First order kinetic constants, half-lives and electrical energy consumption for the degradation of 20 mg L^{-1} CIP by different process.

Process	Degradation efficiency (%) (120 min)	Rate constant (min^{-1})	R^2	$t_{1/2}$ (min)	E_{EO} (kWh m^{-3})
UV	6.57	0.0006	0.9742	1155.33	2048
UV/TiO_2	56.68	0.0063	0.9142	110.03	195.1
UV/TiO_2/MMT	61.70	0.0069	0.8965	100.46	178.1

Table 5
Main chemical and physical composition features of well water.

Parameter	Specification
Appearance	Colorless liquid
Odor	Characteristic
pH	7.82
Conductivity (μS cm^{-1})	323
TDS (mg L^{-1})	226.1
COD (mg L^{-1})	0.8
CL^- (mg L^{-1})	9.83
SO_4^{2-} (mg L^{-1})	19.84
NO_3^- (mg L^{-1})	15.99
NO_2^- (mg L^{-1})	0.04
BrO_3^- (μg L^{-1})	<0.95
Na^+ (mg L^{-1})	6.11
Mg^{2+} (mg L^{-1})	<5
Fe^{2+} (μg L^{-1})	<5
Hardness (mg L^{-1})	152
H_{Ca} (mg L^{-1})	80
H_{mg} (mg L^{-1})	72

TDS: total dissolved solids.
COD: chemical oxygen demand.

The presence of sodium chloride in the aqueous solution had the most inhibiting effect on the photocatalytic activity of TiO_2/MMT, thereby implying that chloride ions scavenged the photo-generated holes and the produced hydroxyl radicals [61,62]. Bicarbonate ions reacted with hydroxyl radicals and produced carbonate radicals [61]. Likewise, bicarbonate ions can scavenge the photo-generated holes [61]. As depicted in Fig. 12, in the presence of sulfate ions in the aqueous solution, the photodegradation efficiency was decreased. The observed retardation effect of sulfate ions was due to adsorbed sulfate ions on the catalyst surface and also, its reaction with photogenerated holes and hydroxyl radicals [63,64]. The potassium iodide was added as the scavenger of both hydroxyl radicals and holes [65,66]. In the presence of iodine anion, a considerable inhibition in photocatalytic degradation was achieved as both hydroxyl radicals and holes were suppressed by iodide ions [67,68].

There are large amounts of ions such as Cl^-, SO_4^{2-}, NO_3^-, NO_2^-, etc. in real water samples which affect the photocatalytic degradation efficiency. In order to investigate the capability of photocatalytic process in the degradation of CIP, the effect of matrix was studied with some well water. Table 5 illustrates the main chemical and physical composition features of the well water. The observed decrease in the CIP degradation efficiency in the well water could be a consequence of the presence of several typical anions (see Table 5). On the basis of these results, it can be concluded that hydroxyl radicals and holes played a determining role in the photocatalytic degradation of CIP.

3.8. The effect of the presence of chemical oxidants

In order to investigate the effect of the presence of the chemical oxidant in the photocatalytic process, the process was carried out in the presence of various chemical oxidant such as hydrogen peroxide, potassium iodate and potassium persulfate. As can be seen from Fig. 13, the presence of hydrogen peroxide, potassium iodate and potassium persulfate resulted in increasing the photocatalytic degradation of CIP from 61.70% to 83.36, 86.43 and 97.88%, respectively. It is obvious that the addition of hydrogen peroxide increased the photocatalytic degradation of CIP due to the increased generation of hydroxyl radicals (Eq. (5)) [29,49].

$$H_2O_2 + h\nu \rightarrow 2OH \quad (5)$$

In addition, the generation of hydroxyl radicals from hydrogen peroxide as electron scavengers was through the following equation [69]:

$$H_2O_2 + e^- \rightarrow OH^- + OH^\bullet \quad (6)$$

Therefore, hydrogen peroxide can be considered as an effective chemical for the generation of hydroxyl radicals to enhance the degradation efficiency [49,70].The addition of potassium iodate can also enhance the photocatalytic degradation efficiency of CIP. The reason is due to the formation of highly reactive radicals and also the capture of the generated electron by this oxidant.

Finally, the addition of peroxydisulfate anion ($S_2O_8^{2-}$) produced the greatest convenient effect on the photocatalytic degradation efficiency. As depicted in Fig. 13, in the presence of $K_2S_2O_8$, the degradation efficiency was increased from 61.70 to 97.8% at the reaction time of 120 min. Each peroxydisulfate ion was activated to generate two SO_4^- radicals under UV radiation (Eq. (7)). Then, hydroxyl radicals could be formed through sulfate radicals as can be seen in Eq. (8) [24,71]:

$$S_2O_8^{2-} + h\nu \rightarrow 2SO_4^{\bullet -} \quad (7)$$

$$SO_4^{\bullet -} + H_2O \rightarrow H^+ + SO_4^{2-} + OH^\bullet \quad (8)$$

3.9. Reusability of the nanocomposite

Fig. 14 shows the results of the reusability test of TiO_2/MMT nanocomposite for the photocatalytic degradation of CIP within five successive cycles with the initial CIP concentration of 20 mg L^{-1}, catalyst dosage of 0.1 g L^{-1} and the irradiation time of 120 min. The photocatalyst in any run was collected, washed with distilled water,

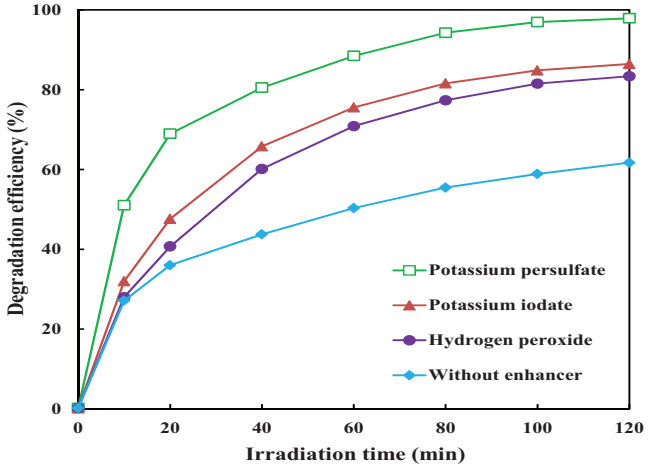

Fig. 13. The effect of different enhancers on the photodegradation efficiency of ciprofloxacin. Conditions: $[Catalyst]_0 = 0.1$ g L^{-1}, $[Enhancer]_0 = 1$ mM, $[CIP]_0 = 20$ mg L^{-1} and pH 5.

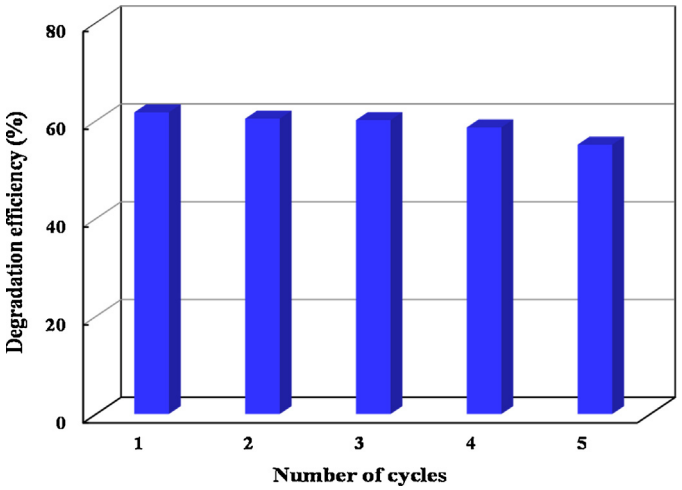

Fig. 14. Reusability of the TiO_2/MMT nanocomposite within five consecutive experimental runs. Conditions: $[Catalyst]_0 = 0.1\ g\ L^{-1}$, $[CIP]_0 = 20\ mg\ L^{-1}$ and reaction time = 120 min.

dried and then used in a new experiment. It could be observed that the degradation efficiency of CIP was decreased slightly from 61.70% to 55.10% after five repeated experimental runs, thereby indicating that the as-prepared TiO_2/MMT nanocomposite could be used as a promising photocatalyst for the degradation of organic pollutants with a significant reusability potential.

3.10. Artificial neural network modeling

It is known that the number of its layers, the number of nodes in each layer and the nature of transfer functions determine the topology of an artificial neural network. In the present work, time (min), initial CIP concentration ($mg\ L^{-1}$), catalyst ($g\ L^{-1}$) and the initial pH were the input variables given to the feed forward three-layered neural network. The degradation efficiency was selected as the tentative response or output variable. Out of several data points generated, 120 experimental sets were employed to feed the ANN structure. The samples were divided into training, validation and test subsets, which contained 72, 24 and 24 samples, respectively. The mean square error (MSE), which was chosen as the function of error performance during the net training process, had the minimum value at 14 neurons among the examined neurons from 2 to 20. Due to the random initialization of the weights, each topology was repeated three times to avoid random correlation. Fig. 15(a) shows the relationship between the mean square error (MSE) and the number of neurons in the hidden layer. As can be seen, the lowest MSE was obtained with 14 neurons. Therefore, 14 neurons were found to represent the best performance of the neural network model. Fig. 15(b) displays the schematic illustration of the optimized ANN structure. Fig. 16, on the other hand, shows a comparison between the values of experimental and predicted degradation efficiency for the test set based on a neural network model. The plot had a correlation coefficient (R^2) of 0.9864 for the output variable of test data set. The correlation coefficient of the plot showed the reliability of the model. The results also revealed that neural network model reproduced the degradation in the present system, within experimental ranges verified in the fitting model. Also, ANN offered the weights that were coefficients between the artificial neurons and therefore, could be considered analogous to synapse strengths between the axons and dendrites in real biological neurons [72].

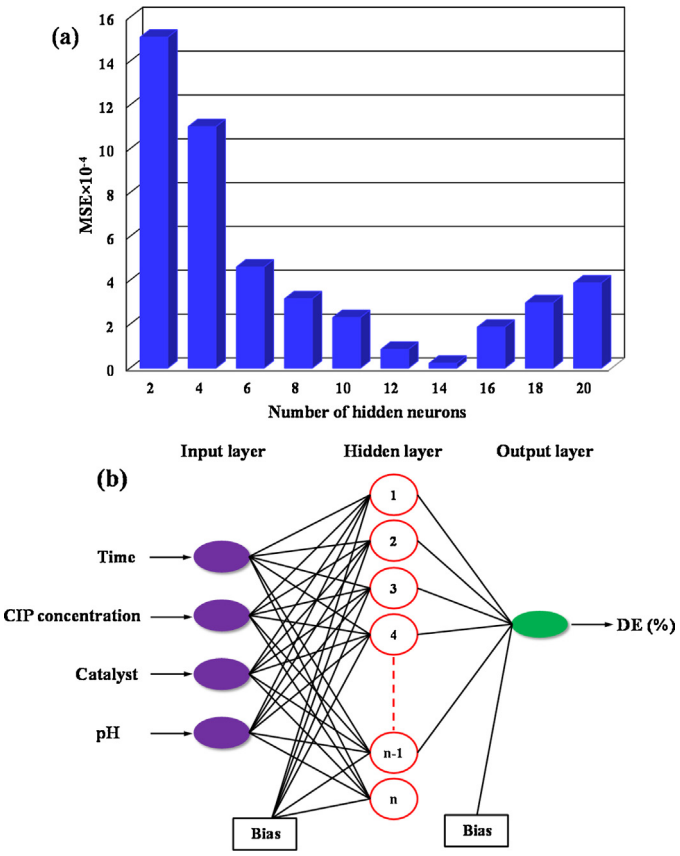

Fig. 15. (a) The effect of the number of neurons in the hidden layer on the performance of the neural network and (b) schematic illustration of the optimized ANN structure.

Table 6 shows the provided weights by ANN in the present study. The effect of each input variable on the output variable was calculated using the neural weight data. The obtained results showed that the relative importance of the initial concentration of CIP, pH of solution and TiO_2/MMT dosage and UV radiation time on degradation efficiency was 30.71, 24.43, 22.55 and 22.31%, respectively. The impact of factors on the degradation efficiency of CIP was also found to be in the following order: CIP concentration > pH > catalyst > time. The CIP degradation efficiency was found to be strongly influenced by all independent variables, but the

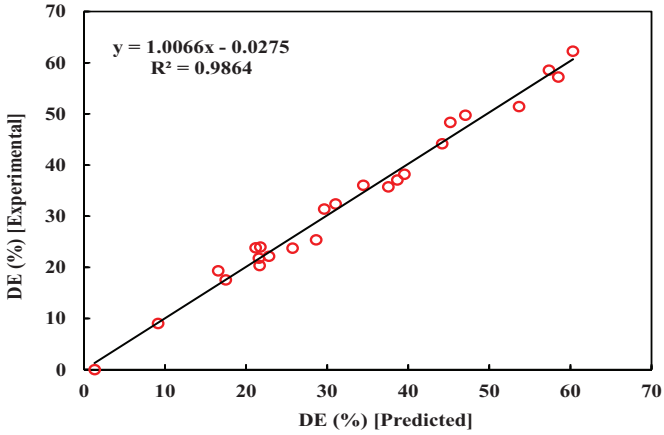

Fig. 16. Comparison of the experimental results with those calculated via neural network modeling for the test set.

Table 6
Matrix of weights, W1: weights between input and hidden layers; W2: weights between hidden and output layers.

Neuron	W1 variable				Bias	W2	
	Time	Concentration	Catalyst	pH		Neuron	Weight
1	1.1229	0.2144	1.8603	1.6026	−2.7032	1	0.2056
2	0.2667	0.9911	−1.3351	−2.1889	-2.1967	2	−0.4648
3	−1.0565	1.1954	1.6084	1.4481	1.8993	3	−0.1897
4	−1.6795	−0.772	1.4683	1.2432	1.5081	4	0.175
5	−0.3288	2.2869	−1.0827	0.8711	1.0871	5	0.2132
6	1.4398	1.6607	0.8649	−1.0486	−0.7822	6	0.6842
7	0.3438	−2.6504	0.0514	0.0019	−0.2667	7	0.6893
8	−2.1303	0.5853	1.4787	−0.0484	0.012	8	0.6841
9	−1.7428	−0.3258	−0.5724	1.956	−0.6419	9	0.0122
10	1.545	−0.4667	−1.6483	1.4195	1.2108	10	0.9178
11	-0.2452	−1.2539	0.4785	2.3491	−1.3744	11	−0.5899
12	−0.6712	1.1937	1.8825	0.9517	−2.0835	12	−0.2002
13	1.126	1.9727	−1.2518	−0.4354	2.3712	13	−0.2641
14	−0.6554	−1.5134	−0.3296	2.1223	−2.7121	14	0.3655
						Bias	−0.1486

Table 7
Identified by-products during photocatalytic degradation of 20 mg L^{-1} CIP at 25 °C after 20 min of reaction at pH of 5.

No.	Compound	t_R(min)	Main fragments (m/z) (%)	Structure
1	Heptyl octyl phthalate	3.00	149.00 (100.00%), 132.90 (77.44%), 446.10 (27.84%), 67.00 (19.47%), 75.00 (18.63%)	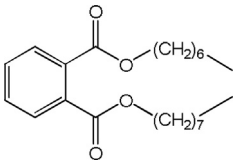
2	1,1,3-Trimethyl-3-phenyl-2,3-dihydro- 1*H*-indene	7.41	221.00 (100.00%), 73.00 (43.76%), 222.00 (22.55%), 103.00 (18.25%), 147.00 (13.79%)	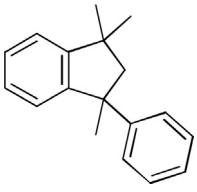
3	3-Methyl-2-propionyl-benzoic acid	2.851	163.00 (100.00%), 133.00 (65.30), 91.00 (37.26%), 59.00 (34.44%), 446.10 (29.25%)	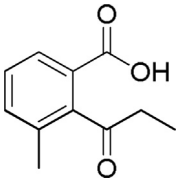
4	3-(2-Hydroxy-2-methylpropyl)cyclohex-2-enone	2.773	59.00 (100.00%), 60.00 (2.85%), 446.20 (1.88%), 55.00 (0.80%), 57.00 (0.67%)	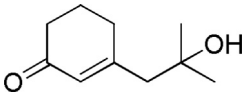
5	Chlorobenzene	3.75	111.90 (100.00%), 77.00 (47.97%), 114.00 (32.79%), 51.00 (13.12%), 75.00 (9.06%)	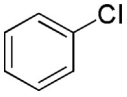
6	Triacontane	27.55	57.10 (100.00%), 55.10 (70.22%), 69.10 (64.72%), 71.00 (62.46%), 97.00 (49.02%)	$CH_3(CH_2)_{28}CH_3$
7	Oleic acid	27.852	57.10 (100.00%), 55.00 (67.92%), 71.00 (66.42%), 69.00 (51.89%), 85.10 (46.31%)	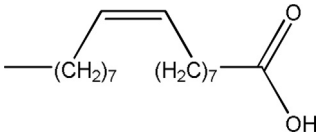
8	*N*,*N*-Dimethylformamide	2.451	73.00 (100.00%), 131.00 (29.05%), 446.10 (20.67%), 146.00 (15.23%), 72.10 (12.28%)	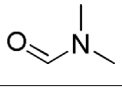

effects of concentration and pH were more noteworthy. Therefore, each of the input variables could not be ignored in the present study.

3.11. Analysis of photocatalytic degradation intermediates of CIP

The intermediates during the first 20 min of CIP photocatalytic degradation were determined using GC-Mass. Eight intermediates with high match factor of mass spectrum were successfully identified (see Table 7). Some of the intermediates have not been detected due to their quick oxidation to the derivatives [53]. Generation of these intermediates during the degradation of CIP emphasizes effective photocatalytic degradation of this pollutant in the presence of TiO_2/MMT nanocomposite.

4. Conclusions

In summary, the photocatalytic degradation of ciprofloxacin was investigated in the presence of immobilized TiO_2 nanoparticles on the surface of MMT. The degradation efficiency of CIP was decreased in initial CIP concentration and increased with increasing TiO_2/MMT nanocomposite dose up to 0.1 g and decreased thereafter. Photocatalytic performance of TiO_2/MMT under UV-C radiation was higher than that under UV-B and UV-A radiation. The efficiency of the studied system in terms of degradation rate followed the order: UV < TiO_2 < TiO_2/MMT < UV/TiO_2 < UV/TiO_2/MMT. Addition of hydrogen peroxide, peroxydisulfate and potassium iodate improved the degradation efficiency. The radical scavenger reduced the degradation efficiency, thereby indicating that the dominant controlling mechanism of photocatalytic degradation of CIP was related to the free radicals. The best degradation was achieved at natural CIP pH (5). Also, after five cycles of repetition use, the degradation efficiency of CIP still remained 55.10%. The electrical energy consumption per order of magnitude for photocatalytic degradation of CIP was the lowest in the UV/TiO_2/MMT process as compared to those in the UV and UV/TiO_2 processes. Artificial neural network (ANN) modeling was successfully used to model the photocatalytic process. All studied factors in this work (time, initial concentration of CIP, catalyst and pH) were found to have remarkable effects on the degradation efficiency.

Acknowledgments

The authors thank to TUBITAK for supports by the 2221-Fellowship Program for Visiting Scientists and Scientists on Sabbatical Leave. The financial support by the Atatürk University Scientific Research Project Council (Project No: 2013/92) is gratefully acknowledged. The authors also thank the University of Tabriz (Iran) for all of the support provided.

References

[1] S. Bae, D. Kim, W. Lee, Appl. Catal. B 134–135 (2013) 93–102.
[2] F.J. Beltrán, A. Aguinaco, J.F. García-Araya, Appl. Catal. B 100 (2010) 289–298.
[3] P. de Voogt, M.-L. Janex-Habibi, F. Sacher, L. Puijker, M. Mons, Water Sci. Technol. 59 (2009) 39–46.
[4] F.J. Beltrán, A. Aguinaco, J.F. García-Araya, A. Oropesa, Water Res. 42 (2008) 3799–3808.
[5] A.R. Khataee, M. Safarpour, A. Naseri, M. Zarei, J. Electroanal. Chem. 672 (2012) 53–62.
[6] A.R. Khataee, M. Fathinia, M. Zarei, B. Izadkhah, S.W. Joo, J. Ind. Eng. Chem. 20 (2014) 1852–1860.
[7] N. Modirshahla, A. Hassani, M.A. Behnajady, R. Rahbarfam, Desalination 271 (2011) 187–192.
[8] S. Khameneh Asl, S.K. Sadrnezhaad, M. Keyanpour Rad, D. Üner, Turk. J. Chem. 36 (2012) 121–135.
[9] M.R. Hoffmann, S.T. Martin, W. Choi, D.W. Bahnemann, Chem. Rev. 95 (1995) 69–96.
[10] A.R. Khataee, M.B. Kasiri, J. Mol. Catal. A: Chem. 328 (2010) 8–26.
[11] F. Sayilkan, M. Asiltürk, Ş. Şener, S. Erdemoğlu, M. Erdemoğlu, H. Sayilkan, Turk. J. Chem. 31 (2007) 211–221.
[12] Y. Li, S.-J. Kim, J. Phys. Chem. B 109 (2005) 12309–12315.
[13] M.S. Vohra, K. Tanaka, Water Res. 37 (2003) 3992–3996.
[14] D. Chen, Q. Zhu, F. Zhou, X. Deng, F. Li, J. Hazard. Mater. 235–236 (2012) 186–193.
[15] A.R. Khataee, M.N. Pons, O. Zahraa, J. Hazard. Mater. 168 (2009) 451–457.
[16] S. Anandan, M. Yoon, J. Photochem. Photobiol. C: Photochem. Rev. 4 (2003) 5–18.
[17] H. Chen, S.W. Lee, T.H. Kim, B.Y. Hur, J. Eur. Ceram. Soc. 26 (2006) 2231–2239.
[18] L. Bouna, B. Rhouta, M. Amjoud, F. Maury, M.C. Lafont, A. Jada, F. Senocq, L. Daoudi, Appl. Clay Sci. 52 (2011) 301–311.
[19] M. Kıranşan, R. Darvishi Cheshmeh Soltani, A. Hassani, S. Karaca, A.R. Khataee, J. Taiwan Inst. Chem. Eng. 45 (2014) 2565–2577.
[20] A. Hassani, R. Darvishi Cheshmeh Soltani, S. Karaca, A.R. Khataee, J. Ind. Eng. Chem. 21 (2015) 1197–1207.
[21] C. Ooka, H. Yoshida, K. Suzuki, T. Hattori, Microporous Mesoporous Mater. 67 (2004) 143–150.
[22] M. Bobu, A. Yediler, I. Siminiceanu, S. Schulte-Hostede, Appl. Catal. B 83 (2008) 15–23.
[23] E. De Bel, J. Dewulf, B.D. Witte, H. Van Langenhove, C. Janssen, Chemosphere 77 (2009) 291–295.
[24] C.-C. Lin, M.-S. Wu, J. Photochem. Photobiol. A 285 (2014) 1–6.
[25] H.-G. Guo, N.-Y. Gao, W.-H. Chu, L. Li, Y.-J. Zhang, J.-S. Gu, Y.-L. Gu, Environ. Sci. Pollut. Res. 20 (2013) 3202–3213.
[26] W.-T. Jiang, P.-H. Chang, Y.-S. Wang, Y. Tsai, J.-S. Jean, Z. Li, K. Krukowski, J. Hazard. Mater. 250–251 (2013) 362–369.
[27] A. Czímerová, J. Bujdák, R. Dohrmann, Appl. Clay Sci. 34 (2006) 2–13.
[28] Y. Bessekhouad, D. Robert, J.V. Weber, N. Chaoui, J. Photochem. Photobiol. A 167 (2004) 49–57.
[29] A.R. Khataee, M.B. Kasiri, J. Mol. Catal. A: Chem. 331 (2010) 86–100.
[30] A.R. Khataee, M. Zarei, M. Pourhassan, CLEAN—Soil, Air Water 38 (2010) 96–103.
[31] F. Rasouli, S. Aber, D. Salari, A.R. Khataee, Appl. Clay Sci. 87 (2014) 228–234.
[32] S. Miao, Z. Liu, B. Han, J. Zhang, X. Yu, J. Du, Z. Sun, J. Mater. Chem. 16 (2006) 579–584.
[33] I. El Younssi, T. Rhadfi, A. Atlamsani, J.-P. Quisefit, F. Herbst, K. Draoui, J. Mol. Catal. A: Chem. 363–364 (2012) 437–445.
[34] Y. Kameshima, Y. Tamura, A. Nakajima, K. Okada, Appl. Clay Sci. 45 (2009) 20–23.
[35] J. Liu, M. Dong, S. Zuo, Y. Yu, Appl. Clay Sci. 43 (2009) 156–159.
[36] J. Liu, X. Li, S. Zuo, Y. Yu, Appl. Clay Sci. 37 (2007) 275–280.
[37] P. Vitanov, A. Harizanova, T. Ivanova, T. Dimitrova, Thin Solid Films 517 (2009) 6327–6330.
[38] A.R. Khataee, M. Sheydaei, A. Hassani, M. Taseidifar, S. Karaca, Ultrason. Sonochem. 22 (2015) 404–411.
[39] Y.L. Pang, A.Z. Abdullah, Chem. Eng. J. 214 (2013) 129–138.
[40] M. Iwasaki, A. Yasumori, S. Shibata, M. Yamane, J. Sol–Gel Sci. Technol. 2 (1994) 387–391.
[41] S. Agarwal, J.N. Ganguli, J. Mol. Catal. A: Chem. 372 (2013) 44–50.
[42] K. Ravi, B. Krishnakumar, M. Swaminathan, Res. Chem. Intermed. 41 (2015) 5353–5364.
[43] S. Miao, Z. Liu, B. Han, H. Yang, Z. Miao, Z. Sun, J. Colloid Interface Sci. 301 (2006) 116–122.
[44] F.-F. Wang, J. Liu, H. Li, C.-L. Liu, R.-Z. Yang, W.-S. Dong, Green Chem. 17 (2015) 2455–2463.
[45] Y. Li, J.R. Liu, S.Y. Jia, J.W. Guo, J. Zhuo, P. Na, Chem. Eng. J. 191 (2012) 66–74.
[46] M. Pirhashemi, A. Habibi-Yangjeh, J. Alloys Compd. 601 (2014) 1–8.
[47] M. Pelaez, N.T. Nolan, S.C. Pillai, M.K. Seery, P. Falaras, A.G. Kontos, P.S.M. Dunlop, J.W.J. Hamilton, J.A. Byrne, K. O'Shea, M.H. Entezari, D.D. Dionysiou, Appl. Catal. B 125 (2012) 331–349.
[48] K. Nakata, A. Fujishima, J. Photochem. Photobiol. C: Photochem. Rev. 13 (2012) 169–189.
[49] N. Daneshvar, D. Salari, A.R. Khataee, J. Photochem. Photobiol. A 162 (2004) 317–322.
[50] M.N. Chong, B. Jin, C.W.K. Chow, C. Saint, Water Res. 44 (2010) 2997–3027.
[51] I.J. Ochuma, R.P. Fishwick, J. Wood, J.M. Winterbottom, Appl. Catal. B 73 (2007) 259–268.
[52] A.R. Khataee, A. Karimi, S. Arefi-Oskoui, R. Darvishi Cheshmeh Soltani, Y. Hanifehpour, B. Soltani, S.W. Joo, Ultrason. Sonochem. 22 (2015) 371–381.
[53] A.R. Khataee, S. Arefi-Oskoui, M. Fathinia, A. Esmaeili, Y. Hanifehpour, S.W. Joo, N. Hamnabard, J. Mol. Catal. A: Chem. 398 (2015) 255–267.
[54] F.J. Beltrán, F.J. Rivas, O. Gimeno, J. Chem. Technol. Biotechnol. 80 (2005) 973–984.
[55] J.-h. Sun, Y.-k. Wang, R.-x. Sun, S.-y. Dong, Mater. Chem. Phys. 115 (2009) 303–308.
[56] James R. Bolton, Keith G. Bircher, William Tumas, C.A. Tolman, Pure Appl. Chem. 73 (2001) 627–637.
[57] J.A. Cortés, M.T. Alarcón-Herrera, M. Villicaña-Méndez, J. González-Hernández, J.F. Pérez-Robles, Environ. Prog. Sustain. Energy 30 (2011) 318–325.
[58] N. Carmosini, L.S. Lee, Chemosphere 77 (2009) 813–820.
[59] T.A. Gad-Allah, M.E.M. Ali, M.I. Badawy, J. Hazard. Mater. 186 (2011) 751–755.
[60] N. Daneshvar, S. Aber, M.S. Seyed Dorraji, A.R. Khataee, M.H. Rasoulifard, Sep. Purif. Technol. 58 (2007) 91–98.

[61] D.E. Santiago, J. Araña, O. González-Díaz, M.E. Alemán-Dominguez, A.C. Acosta-Dacal, C. Fernandez-Rodríguez, J. Pérez-Peña, J.M. Doña-Rodríguez, Appl. Catal. B 156–157 (2014) 284–292.
[62] P.-S. Yap, T.-T. Lim, Appl. Catal. B 101 (2011) 709–717.
[63] M. Sökmen, A. Özkan, J. Photochem. Photobiol. A 147 (2002) 77–81.
[64] A.R. Khataee, Environ. Technol. 30 (2009) 1155–1168.
[65] J. Rabani, K. Yamashita, K. Ushida, J. Stark, A. Kira, J. Phys. Chem. B 102 (1998) 1689–1695.
[66] L.-S. Zhang, K.-H. Wong, H.-Y. Yip, C. Hu, J.C. Yu, C.-Y. Chan, P.-K. Wong, Environ. Sci. Technol. 44 (2010) 1392–1398.
[67] R. Palominos, J. Freer, M.A. Mondaca, H.D. Mansilla, J. Photochem. Photobiol. A 193 (2008) 139–145.
[68] K.-i. Ishibashi, A. Fujishima, T. Watanabe, K. Hashimoto, J. Photochem. Photobiol. A 134 (2000) 139–142.
[69] B.J.P.A. Cornish, L.A. Lawton, P.K.J. Robertson, Appl. Catal. B 25 (2000) 59–67.
[70] N. Modirshahla, M.A. Behnajady, R. Rahbarfam, A. Hassani, CLEAN—Soil, Air Water 40 (2012) 298–302.
[71] A.R. Khataee, R. Darvishi Cheshmeh Soltani, Y. Hanifehpour, M. Safarpour, H. Gholipour Ranjbar, S.W. Joo, Ind. Eng. Chem. Res. 53 (2014) 1924–1932.
[72] A. Hassani, F. Vafaei, S. Karaca, A.R. Khataee, J. Ind. Eng. Chem. 20 (2014) 2615–2624.